Acta Biomaterialia 159 (2023) 74–82

Contents lists available at ScienceDirect

Acta Biomaterialia

journal homepage: www.elsevier.com/locate/actbio

Full length article

# On stars and spikes: Resolving the skeletal morphology of planktonic Acantharia using synchrotron X-ray nanotomography and deep learning image segmentation

Dawn Raja Somu[a], Timothy Cracchiolo[a], Elena Longo[b,c], Imke Greving[b], Vivian Merk[a,*]

[a] Department of Chemistry and Biochemistry, Department of Ocean and Mechanical Engineering, Florida Atlantic University, Boca Raton, FL, United States
[b] Institute of Materials Physics, Helmholtz-Zentrum Hereon, Geesthacht, Germany
[c] Elettra-Sincrotrone Trieste S.C.p.A., Basovizza, Trieste, Italy

ARTICLE INFO

*Article history:*
Received 3 October 2022
Revised 13 January 2023
Accepted 17 January 2023
Available online 25 January 2023

*Keywords:*
Biomineralization
Crystallization
X-ray nanotomography
Deep learning image segmentation
Strontium sulfate
Biomaterials
Biointerface
Morphogenesis

ABSTRACT

Acantharia (*Acantharea*) are wide-spread marine protozoa, presenting one of the rare examples of strontium sulfate mineralization in the biosphere. Their endoskeletons consist of 20 spicules arranged according to a unique geometric pattern named Müller's principle. Given the diverse mineral architecture of the Acantharia class, we set out to examine the complex three-dimensional skeletal morphology at the nanometer scale using synchrotron X-ray nanotomography, followed by image segmentation based on deep learning methods. The present study focuses on how the spicules emanate from the robust central junction in the orders *Symphyacanthida* and *Arthracanthida*, the geometry of lateral spicule wings as well as pockets of interspicular space, which may be involved in cell compartmentalization. Through these morphometric studies, we observed subtle deviations from the previously described spatial arrangement of the spicules. According to our data, spicule shapes are adjusted in opposite spicules as to accommodate the overall spicule arrangement. In all types examined, previously unknown interspicular interstices were found in areas where radial spicules meet, which could have implications for the crystal growth mechanism and overall endoskeletal integrity. A deeper understanding of the spiculogenesis in Acantharia can provide biomimetic routes towards complex inorganic shapes.

**Statement of significance**

Morphogenesis, the origin and control of shape, provides an avenue towards tailored inorganic materials. In this work, we explored the intricate skeletal organization of planktonic Acantharia, which are amongst the few strontium sulfate biomineralizing organisms in nature. By using nanoscale X-ray imaging and deep learning image segmentation, we found deviations from previously described geometric patterns and undiscovered skeletal features. The bio-inspired synthesis of inorganic materials with complex shape has important ramifications for solid-state chemistry and nanotechnology.



## 1. Introduction

The underlying mechanisms by which living organisms build complex mineral architectures in accordance with the symmetry of the crystal lattice remains enigmatic. Morphogenesis describes the origin and control of complex inorganic shapes and morphological patterns that span multiple length scales [1–5]. Key principles of inorganic pattern formation are supramolecular assembly, molecular recognition, templating, and hierarchical organization [1,6,7]. Among the myriad of inorganic materials produced by organisms, single crystals are common skeletal elements across the kingdoms of life [8]. Based on a more profound understanding of such biological systems, we may devise straightforward strategies for the growth of single crystals with desired size, form, perfection, and homogeneity [9]. This knowledge is particularly useful in finding sustainable routes to growing synthetic single crystals from aqueous solution at ambient temperature. Smoothly curving single crystals, as exemplified by the Acantharia, are a rich source of inspiration to inorganic materials used as catalysts, solar cells, energy storage media or medical implants [10–13].

Acantharia (*Acantharea*) are single-celled marine protozoa that present one of the rare examples of strontium sulfate ($SrSO_4$, ce-

* Corresponding author.
*E-mail address:* vmerk@fau.edu (V. Merk).

https://doi.org/10.1016/j.actbio.2023.01.037
1742-7061/

lestite) mineralization in the biosphere [14–17]. These planktonic organisms occupy a unique ecological niche by selecting strontium ions over chemically similar, but more abundant calcium ions from seawater. Apart from being an integral part of the marine ecosystem [18], Acantharia play a major role in biogeochemistry by controlling strontium and barium fluxes [19–21] and contributing to oceanic carbon and nitrogen cycles [22]. Although Acantharia are common subsurface plankton species across the globe, ranging from polar to tropical climate zones, a pattern of seasonality exists in most places [18,21–23].

Acantharia are a class within the radiolarians in the eukaryotic super-group Rhizaria that encompasses approximately 50 genera and 150 species with highly diverse skeletal morphology, which is consistent with fine genetic regulation of the mineral deposition [24,25]. The size of the skeleton is on the order of 50 $\mu$m to 1 mm, depending on the developmental stage and geographic origin. Contingent on the molecular clade, the skeleton consists of either 10 diametral (clades A and B) or 20 radial spicules (clades C-F). Acantharia from clades A and B do not form a central junction, but the spicules loosely cross the center of the cell. In clade C, the 20 spicules are connected by contractible fibrils, giving rise to a foldable umbrella-like structure. The present study focuses on the taxonomic suborders *Symphyacanthida* and *Arthracanthida* (molecular clades E and F), which are characterized by a high degree of morphological complexity and a robust central junction that fixes the spicules in the center of the cell.

Acantharia from clades E and F follow a sophisticated symmetrical arrangement, generally known as Müller's principle. The geometric law states that two quartets of polar spicules alternate with two quartets of tropical spicules and one quartet of equatorial spicules [14,26,27]. This geometric organization was originally thought to be governed by the space-efficient packing of the vesicles enclosing the spicules [28]. While Müller's principle describing the geometrical arrangement of the Acantharian spicules has been known for over a century [14], it is yet poorly understood how exactly spicules fuse in the center of the organism. In the quest of explaining morphogenesis in nature [28], D'Arcy Thomson suggested in his landmark monograph "On Growth and Form" that the twenty Acantharian spicules radiate towards the faces of an icosahedron [28]. Perry *et al.* speculated that the arrangement of the spicules stems from an interplay between crystallochemical and biological control, reconciling an optimum use of space at the spicular joint with the crystallographic requirements of an orthorhombic crystal lattice [27,29]. However, as illustrated by Wilcock *et al.* [28] and explored in this study, the spatial arrangement of the 20 spicules do not exactly follow this arrangement, but rather loosely adhere to Müller's principle.

The curved surface of the Acantharian spicules is at odds with the internal lattice structure of the orthorhombic crystal. Apart from sculpting the crystal shape, Acantharia exert exquisite control over the crystallographic texture. As previous studies indicate, spicules grow along the crystallographic *a*-axis, with the lateral wings consistently lying in low-index planes, irrespective of the skeletal morphology [27]. In contrast, geological $SrSO_4$ crystals grown under equilibrium conditions are aligned along the crystallographic *c*-axis [27,30].

Acantharia exhibit a fascinating diversity in spicule shapes. It is known that celestite crystallization occurs in membrane-bound vesicles known as perispicular vacuoles that restrain crystal growth [27]. Previous research reported that spicules are joined to each other with protoplasmic strands called “spicular cement” [31]. The spicule-containing compartments are attached to both the cytoplasmatic membrane and microtubule filaments [27,29]. Hence, the evolution of the spicule shape has hitherto been attributed to the different growth rates of cellular constituents, namely a higher growth rate of the vesicle containing the developing spicule compared to the overall cell [29]. This hypothesis implies that the spatial organization of membranes and filaments, in particular the filament length and cell membrane curvature, accounts for the spicular crystal shape [29], but it falls short of explaining apparent taxon-specific variations in spicule morphology, which might be influenced by intracrystalline matrix proteins, as observed in other biomineralizing organisms, such as sea urchin larvae [32]. In some Acantharian species, both vesicle and cell membrane start growing tangentially along the cell surface when the spicules touch the capsular membrane, producing a porous inorganic $SrSO_4$ shell enclosing the amoeboid body [33,34].

In contrast to many other biomineralizing organisms, Acantharia are uncultured protists that cannot be kept in the laboratory for an extended time after capture [31,34]. In most sampling locations, Acantharia need to be harvested from the open ocean using Niskin bottles, scuba divers, plankton nets, or sediment nets [22,35]. Another potential hurdle in the study of these planktonic organisms is that the celestite skeleton dissolves rapidly in high salinity seawater upon cell death [35,36]. As a result, this marine life form is absent from the fossil record [19]. Hence, suitable fixation methods are required to preserve the delicate skeleton for further analysis, including the conservation in ethanol, formaldehyde solution, cryo-fixation, or freeze-drying [37,38]. Due to the challenges to preserve the organic matter by ethanol over an extended time period, the present study focuses on the mineral architecture. Moreover, the poor stability in culture renders time-resolved studies of the spiculogenesis across developmental stages impossible. Previous research showed that the unique mineralization patterns evolve through primitive stages in juvenile Acantharia, in which rod-shaped, diametral spicules cross in the center of the cell before elaborating towards well-developed skeletons in the adult [24,26,27,29].

To resolve the complex internal morphology of Acantharian endoskeletons, we used synchrotron-based X-ray nano-computed tomography (X-ray nanoCT) at the P05 imaging beamline (PETRA III, DESY, Hamburg, Germany). X-ray nanoCT is a powerful imaging tool for visualizing internal and external nanostructures in a non-destructive manner [39,40,41], thereby avoiding sample preparation artefacts from sectioning a priori [42,43]. Here, the resolution of the hard X-ray microscope exceeded 50 nm. The high linear absorption coefficient of strontium sulfate rendered Acantharia ideal samples for nanofocused X-ray imaging. Detailed reconstructions of the X-ray tomographic data based on variations of the linear attenuation coefficient allowed us to perform exact morphometric measurements, e.g., interspicular angles. In addition, volume renderings were digitally rotated and analyzed from different points of view. Based on the experimental results, we gained a deeper understanding of the skeletal development in Acantharia. Special emphasis was placed on taxon-specific features, such as the complex morphology of the inner joint, as these parts are likely to be involved in the oriented growth of $SrSO_4$ crystals.

## 2. Materials and methods

### 2.1. Data collection

A mixed assemblage of planktonic organisms collected using net tows at Mborokua, Solomon Islands, and preserved in 70% (v/v) aqueous ethanol was kindly provided by the American Museum of Natural History (New York, New York). In the present study, we primarily focused on Acantharia from the orders *Symphyacanthida* and *Arthracanthida* (molecular clades E & F) that are characterized by their robust central junction and intricate skeletal morphology. Since the cellular matter was not preserved by the alcohol, samples were classified based on morphological cues. However, an unambiguous taxonomic identification would re-

quire molecular phylogenetic information [34]. Prior to X-ray imaging, Acantharia were treated with 8.25% NaOCl for 30 min to remove surrounding organic material, was hed with $H_2O$ and 95% ethanol. 1 mm quartz capillaries (Charles Supper) were used for pulling glass fibers. To prevent glass absorption, Acantharian endoskeletons were mounted on the tip of pulled glass needles using cyanoacrylate glue (Super Glue, 3 M) under a Zeiss Stemi 2000-C stereomicroscope and held in place by a screw-in sample holder.

In this study, over 20 Acantharian endoskeletons were scanned using synchrotron radiation nano-computed tomography at beamline P05 operated by the Helmholtz-Zentrum Hereon at the PETRA III storage ring at DESY (Deutsches Elektronen-Synchrotron, Hamburg, Germany) [44]. A Fresnel zone plate (FZP) was used as an objective lens. An X-ray sCMOS camera (Hamamatsu C12849–101 U, 6.5 mm pixel size, 2048×2048 pixels, 16-bit image depth) with a 10 µm Gadox scintillator was used as a detector. Using this setup, a pixel size of 13 nm and a spatial resolution of 50 nm were achieved at 11 keV in 2D [45]. In this study, two different setups were used: In the first setup, a large FZP of 250 µm was employed to achieve a larger field of view of 74 µm, resulting in an effective pixel size of 35.94 nm. The other setup featured a 150 µm diameter FZP, resulting in an effective pixel size of 18.65 nm and a field of view of 38 µm. Samples were scanned using a monochromatic beam with X-ray photon energy of 11.1 keV. Each scan consisted of 1600–3200 radiographs over 180° with an exposure time of 1.1 s per projection (smearing = 1, speed = 0.1°/s). Due to the high absorption coefficient of $SrSO_4$, scans were performed with total scan times from 30 min to 1 h in standard absorption mode. The quality of the tomographic reconstruction tends to scale with the number of projections, but we noted only minor differences between 30 min and 1 h scans. A prolonged scan time may in fact undergo with significant sample drift of the sample. Due to the high X-ray absorption coefficient of the strontium-bearing mineral, nanoCT data were obtained in absorption mode. Scans were normalized by flatfield radiographs and corrected for dark current using in-house code and were reconstructed with the Gridrec algorithm [46] using the TomoPy package and a binning size of 2, doubling the effective pixel size [47]. Reconstruction of nanoCT data was carried out using an in-house beamline script. The reconstructed data was used to carry out virtual slicing of the endoskeleton. The reconstructed scan data (stack of 2D slices) were imported into the 3D visualization and analysis software Dragonfly (Object Research Systems Inc, Montreal, Canada, 2020, Version 2020.2) for Windows. 3D Models of Acantharian endoskeletons were made from the reconstructed nanoCT data using Dragonfly's deep learning module.

### 2.2. Image segmentation using deep learning methods

The reconstructed image stacks were edited in preparation for AI segmentation using the Image Filtering workspace in Dragonfly. Image contrast was enhanced via histogram equalization, and smoothed using mean shift, gaussian, and percentile smoothing methods. 10–20 projections in the XY plane were segmented manually and were used as training data. U-Net Convolutional Network for Biomedical Image Segmentation was used as the algorithmic architecture for the segmentation for each of the ten samples [48]. The data was segmented into two regions of interests: the Acantharian endoskeleton and the background. The endoskeleton ROIs were saved as .tiff stacks to create 3D models and videos, and for determining interspicular angles.

### 2.3. Angle measurement

The 3D models generated from the AI-assisted image segmentation of the nanotomography data were loaded into 3D Slicer. [49] For each Acantharian endoskeleton model, the center of the cross-section of each spicule as well as the center of the overall model were annotated using points. Each spicule was also given a "polar," "tropical," or "equatorial" assignment as per Müller's principle. The polar and tropical assignments were further labelled "north" and south," with the hemispheres arbitrarily assigned for ease of angle measurement. This resulted in five spicule assignments: PN, TN, EQ, TS, and PS. The points and the spicule arrangements were imported into a custom MATLAB live script through which interspicule angles were determined. This was accomplished by first fitting a sphere at the center of the spicule junction, and then determining the intersection of each spicule vector with the sphere, such that the spicule length for all the spicules in each model was the same. Using these new spicule vectors, an ellipse was fit around each of the five spicule assignments. The centers of these ellipses were used to make a non-spicule "central vector." Two types of angles were measured: the angle between each spicule and the central vector (Fig. 1, i), as well as the angle between an equatorial spicule in the sample and all the other spicules as projected onto the equatorial plane (Fig. 1, ii). Additional information on angle measurement can be found in the supplemental information. Statistical analyses were carried out using the Data Analysis ToolPak on Microsoft Excel (2020).

## 3. Results and discussion

### 3.1. Morphology of spicule junctions

Acantharian endoskeletons consist of 20 spicules, specifically four pairs of polar (P) spicules, four pairs of tropical (T) spicules, and two pairs of equatorial (E) spicules. As illustrated in Fig. 1, Müller's principle states that all equatorial spicules are at right angles towards each other. Tropical spicules are oriented at a 30° angle from the equatorial plane while being rotated 45° from the equatorial spicules when viewed from above. Polar spicules protrude at 60° angles from the equatorial plane, thereby overlapping with the equatorial spicules [14]. A stereographic projection of spicular arrangement is shown in Figure S1.

The present study focuses on how the spicules emanate from the central junction and whether the three-dimensional arrangement of spicules deviates from Müller's principle in morphologically complex Acantharia. The central junction was of special interest, since the arrangement of the spicules towards the center of the endoskeleton could provide insight into how loose spicules fuse together during the developmental stage of the organisms. To test the validity of the geometric law, polar, tropical,

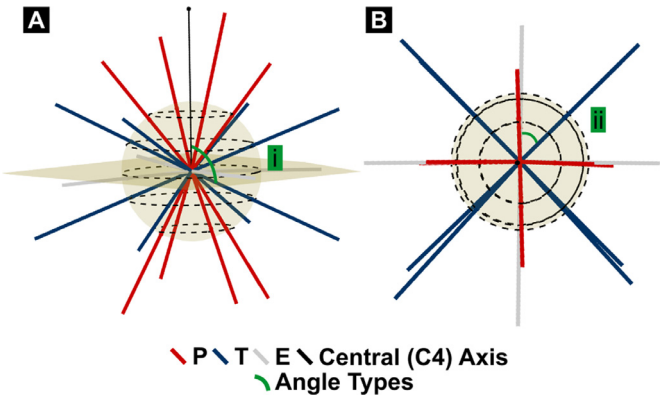


**Fig. 1.** Schematic of geometric arrangement of spicules as per Müller's principle; $P$ = polar spicules, $T$ = tropical spicules; $E$ = equatorial spicules. Left: Each line represents one of 20 radial spicules. The plane containing equatorial spicules shown. Right: View along central axis. The two types of interspicular angles measured in this study are indicated using (i) and (ii).

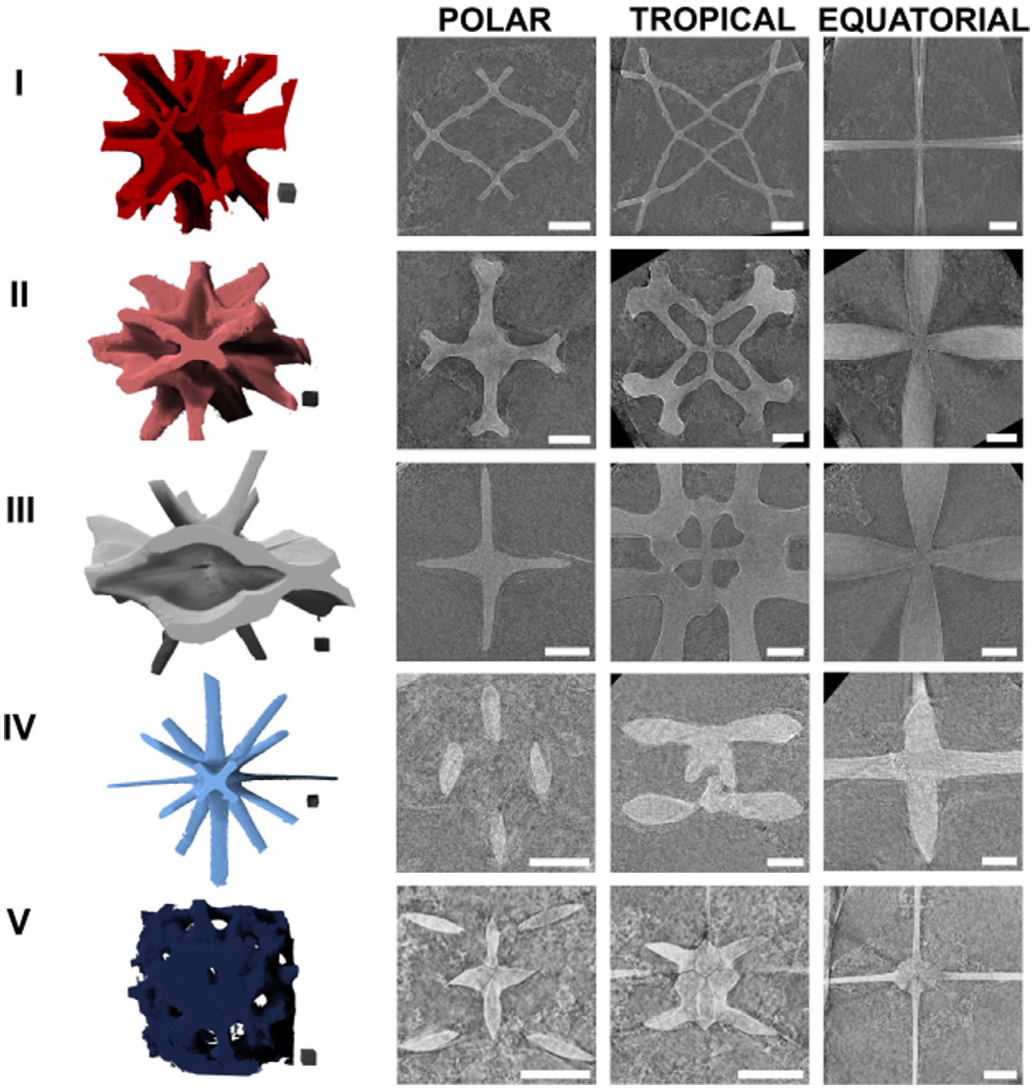


**Fig. 2.** Diverse morphology of spicule junction. Type I: Lateral wings for all spicules. Type II: Lateral wings for two spicules. Type III: Less pronounced lateral wings for all spicules. Type IV: Lateral wings only on one pair of equatorial spicules. Type V: Presence of porous shell. Left: 3D segmentation models from type I-V endoskeletons. Cube in bottom right corner of each model has length of 5 $\mu$m. Models are falsely colorized. Right: 2D NanoCT reconstructed slices for polar, tropical and equatorial spicules. Scale bars correspond to 10 $\mu$m.

and equatorial spicules were assigned as per Müller's principle, their spatial orientation was converted to vectors centered at (0,0,0) and the suitability of the assignment was verified using a custom MATLAB script. In all samples examined in this experiment, the polar, tropical, and equatorial spicules oriented with similar interspicular angles to those dictated by Müller's principle. Yet, while the overall spatial arrangement was maintained across the samples to a large extent, there were stark differences in terms of spicule shape and thickness between different types. Image segmentations based on Deep Learning Models were used to create three-dimensional volume renderings. The twenty endoskeletons that were examined as part of this study were classified according to morphological similarities. We further observed pronounced differences with regard to how the spicules fused in the central junction between different species. Based on differences in these criteria, the samples examined were divided into five types to ease discussion of morphological differences between samples. These types, along with projections of how the polar, tropical, and equatorial spicules meet are presented in Fig. 2. The region of the 3D model from which the planar views of the spicular junctions in Fig. 2 are presented in Figure S2. 3D views of the polar, tropical, and equatorial junctions are shown in Figure S3.

Type I samples are characterized by 20 thin radial spicules with cruciform cross sections, which stem from the presence of lateral wings on all spicules. Acantharia from the family *Acanthometridae* (Genus *Amphilonche*) have 20 spicules with four-winged cross-section near the base. Due to this particular spicule shape, an opening remains in the middle where the four polar spicules join. Two of the four lateral projections from each polar spicule meet with one projection of two other polar spicules. The two other initially unattached ends of the polar spicules merge with the tropical spicules. Gaps are again maintained in the center of the tropical junctions which do not close fully until the four equatorial spicules merge in the middle of the endoskeleton. These gaps could result in an overall weaker, yet more lightweight endoskeleton, creating additional interspicular compartments lined by the mineralized endoskeleton, which could be necessary for the sequestration of organelles or harboring the cytoplasm. The four equatorial spicules meet each other at right angles, as per Müller's principle. The spicules appear to narrow down almost to a point as they meet in the middle, as observed in other studies [27,50]. Unlike the endoskeleton of the simpler Acantharian species *Phyllostaurus siculus* studied by Wilcock *et al.* [27], in which spicules also connect to each other via lateral wing structures, here there are four lateral

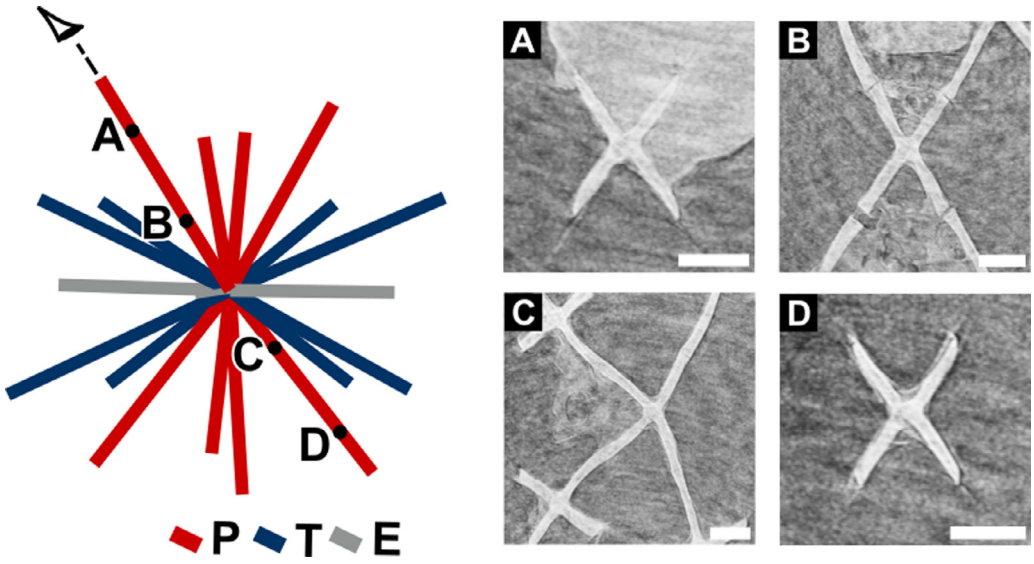


**Fig. 3.** Diametric variation in spicule cross-section. Left: Schematic of 3D spicular arrangement with polar (P, red), tropical (T, blue) and equatorial (E, gray) spicules. Right: Progression of 2D projections illustrate change in shape within an individual polar spicule and in diametric polar spicule of Type I sample. Scale bar corresponds to 5 µm.

wings present on all spicules in the samples of this type. Additionally, the orientation of the lateral wing as well as the shape of the spicule cross-section are not maintained diametrically, especially for the polar spicules of this type (Fig. 3). The spicule shape is adjusted as required to maintain the overall spatial arrangement of the spicules. Wilcock *et al.* hypothesized that the availability of space near the poles (or lack thereof) influences the arrangement of the lateral wings [27]. Since the lateral wing placement of four out of the eight Type I polar spicules resemble tropical spicules and the other four resemble equatorial spicules, the spatial constraint appears to be adjusted for by the alternation of lateral wing arrangement in two out of polar spicules at each polar junction.

Of all the samples examined, the lateral wing arrangements of the Type II samples most closely resemble that of the species *P. siculus* (Family *Phyllostauridae*, Genus *Phyllostaurus*) studied by Wilcock et al. [27]. *P. siculus* is furnished with 20 cylindrical spicules, yet, the proximal ends of the radial spicules are cross-shaped. The spicule cross-sections are thicker overall and more rounded compared to those of the Type I samples. At the polar junction where the polar spicules first meet, as shown in Fig. 2, the spicules fuse without an obvious gap outside of the small interspicular spaces (addressed later in this paper). This suggests that the central axis of this type of Acantharia is more strongly reinforced compared to the type I samples. Video 1 highlights how the different spicule types, specifically polar (red), tropical (blue), and equatorial (beige), fuse together as they approach the central junction for this sample type.

2D slices of the reconstructed nCT volume of the Type III samples resemble that of the Type II samples, but Type III samples feature deeper interspicular compartments and thinner polar spicules. In this type (Family *Diploconidae*, Genus *Diploconus*), the tropical spicules fuse with the equatorial spicules, and combined, the two types of spicules form a cornet, a mineralized skirt around the equatorial plane encasing the entire central junction. This is especially evident in a tomography with a smaller voxel size (~35nm), which looks more closely at the central junction (Video 2). Lateral wings are present on all spicules but are less pronounced in the polar spicules, particularly in the 3D representation of the sample.

The endokeletons of Type IV and Type V samples have porous shells around the central junction. Latticed or armored shells are commonly found in the families *Dorataspidae* and *Dictyacanthidae*. In Type IV samples, only one pair of equatorial spicules has four lateral wings and the resulting cross-shaped spicule cross section, while the remaining spicules have an ovalish cross section. The other pair of equatorial spicules are not particularly larger in size compared to the remaining 16 spicules, thereby retaining oval-shaped cross-sections. In the area of the central junction examined in the nanotomography experiment, the shells of the Type IV samples were not visible.

Type V samples are equipped with a porous shell surrounding the central junction. None of the twenty radial spicules in the imaged samples have lateral mineralized wings present, and as such, all their cross-sections are roughly oval-shaped. Towards the central junction, the spicules become more angular as they almost reach out to the other spicules, but do not have any apophyses (mineral protuberances) compared to the previous types examined. The lack of cross-shaped or ridged spicules for the shelled samples could point to the two structural features, shells and ridged spicules, being formed through a similar growth mechanism. The central junction of these samples also appears to have some extra reinforcement in the middle compared to the other types, as there are traces of short stubs of the tropical spicules remaining in the very center. This could be due to equatorial spicules in Type V samples being the thinnest of all the types, and therefore they could require additional reinforcement to hold all the spicules in their arrangement as the organism moves, without compromising the stability of the central junction.

### 3.2. Diametric variation in spicule cross-section

We further addressed the question as to how the spicule cross-section changes along a pair of diametric spicules. In an exemplary manner, Fig. 3 displays changes in the x-shaped cross-section of polar spicules in a type I endoskeleton where all 20 spicules are furnished with lateral wings. Morphometric measurements along opposite spicules reveal that the orientation of the lateral wings as well as the shape of the spicule cross-section are not maintained within an individual spicule as well as in diametric spicules. As we move from the tip of a spicule towards the central junction, the x-shape converges to a point at the very center of the endoskeleton, potentially due to space constraints, as exemplified by tomographic slices from the spicule cross section close to the tip (Fig. 3A,D) or the central junction (Fig. 3B,C). Similarly, spicules of type II morphology become more angular as they approach

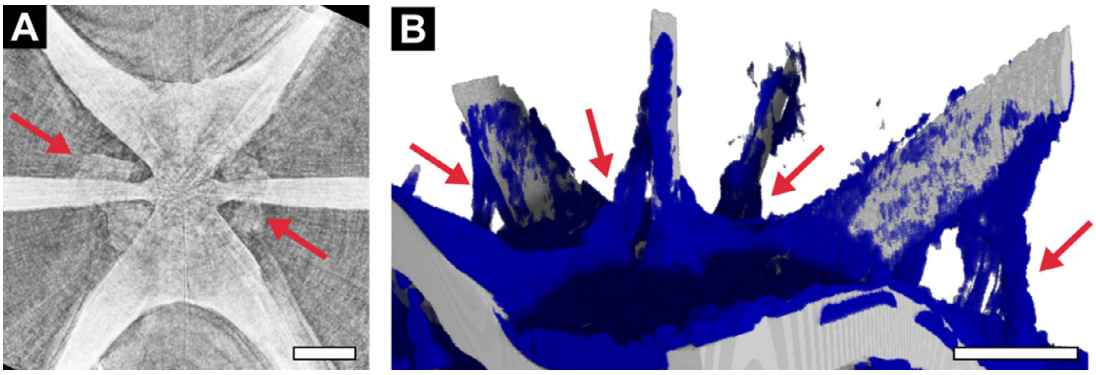


**Fig. 4.** Mineralization pattern surrounding the spicules of a type III endoskeleton marked by red arrows. (A) indicates the presence of such material towards the center of the Acantharia. (B) shows the material acting like struts connecting the polar spicules to the other spicules in 3D. Scale bars correspond to 10 µm.

the central junction and more ellipsoidal away from the center. We hypothesize that the spicule shape is adjusted as required to maintain the overall spatial arrangement of the 20 spicules.

### 3.3. Mineralization pattern around central junction

Based on variations in X-ray absorption coefficient, we can easily discern mineralized from unmineralized regions. Surrounding the central joint, we found X-ray absorbent areas, which are not part of the endoskeleton. Such regions may serve as mineral reservoirs or precursor mineral phases preceding the fully mineralized skeletal elements. Skeletal formation processes, such as ion accumulation, mineral deposition and reorganization are likely to occur in the unicell center. Furthermore, unmineralized pockets bulge inwards towards the central joint, providing additional space for cellular organelles. This is illustrated in Video 3, where a sphere mask of progressively decreasing radius is applied to a 3D model of the endoskeleton of a Type II sample. In Type III samples, spicule fusion results in a mineralized plane with deep pockets around the central junction (see red arrows in Fig. 4A). X-ray absorbent material surrounds the spicules, potentially acting as support struts for the polar spicules or previously observed “spicular cement” [31], as depicted in Fig. 4B.

### 3.4. Interspicular interstices

In the areas where radial spicules meet each other or fuse, we found interspicular interstices such that the spicules can still be distinguished as separate crystals even in the central junction where all twenty spicules fuse together. As depicted in Fig. 5, these interstices were found in all five types of samples, suggesting that they are not image artefacts. The interstices show remarkable symmetry in arrangement, as shown in Fig. 6. Previous research demonstrated that each Acantharian spicule is a single crystal, which likely originates from an individual nucleation event inside its vesicular compartments [26,27,29]. Based on our observations and contrary to previous literature reports [31], the spicules do not completely merge in the center, but they remain separate entities. The spicule interstices range from roughly 70 nm to 200 nm in length and stretch along the entire width of the region where any two spicules fuse. The size of these interstices is largely consistent in size across types but reached up to 800 nm in one Type I sample. An advantage of nanofocused X-ray imaging consists in the high resolution necessary to resolve such fine skeletal features as well as the nondestructive nature of the experimental approach. Since interspicular gaps are reminiscent of growth plates in immature bone [51], their presence might provide new perspectives on $SrSO_4$ spiculogenesis across developmental stages.

### 3.5. Interspicule angle measurements

Of the samples examined, the interspicular angles of five samples of Type I, one sample of Type II, two samples of Type IV, and two samples of Type V were thoroughly measured. Angle measurements were not carried out for Type III samples as the tropical spicules were not clearly distinguishable from the lateral wings of the equatorial spicules of these samples within the scanned area.

#### 3.5.1. Angles measured from central (non-spicule) axis

To examine possible deviations from Müller’s principle, the angle between a central non-spicule axis (the C4 axis, illustrated in Fig. 1) and all spicules was measured and compared by sample type in Table 1. For all sample types examined, the angle between this central vector and a polar spicule is around 35º, whereas the angle between this axis and a tropical spicule is around 67º, rather than an evenly portioned 30º and 60º for polar and tropical spicules respectively. These results contradict recent findings by Fujimaki *et al.* who focused on the three-dimensional arrangement of four-bladed spicules in *Acanthometra* cf. *multispina* [50] (Family *Acanthometridae*). Wilcock *et al.* inferred interspicular angles from a combination of optical microscopy, SEM and electron diffraction [27]. Our experimental approach based on nanofocused X-ray tomography revealed subtle deviations from Müller’s principle in morphologically complex Acantharian skeletons. We believe that the high spatial resolution and nondestructive nature of the imaging technique helped improve the accuracy of the morphometric measurements.

#### 3.5.2. Angles measured from equatorial plane projections

The interspicular angles here were thoroughly measured from one of the four equatorial spicules to all the projections of all spicules onto the equatorial plane. It is expected according to Müller’s principle that polar angles projected onto the equatorial plane would lie on top of the equatorial angles, at 0º, 90º, or 180º measured either side from the chosen equatorial spicule. Likewise, the projections of the tropical spicules are expected to lie at 45º or 135º either side of the equatorial spicule. Table 2 shows that the angles measured differ on average from these expected values by around 3º for each type. This result suggests that while there are some spatial restraints as described by Müller’s principle, there is some room for variation in how the spicules can be oriented in space, depending on the unique spicular morphology. Since only one Type II sample was examined, the results were more easily skewed. We conclude that the three-dimensional arrangement of spicules is dictated by space restraints at the central junction together with the crystallographic requirements of the orthorhombic crystal lattice.

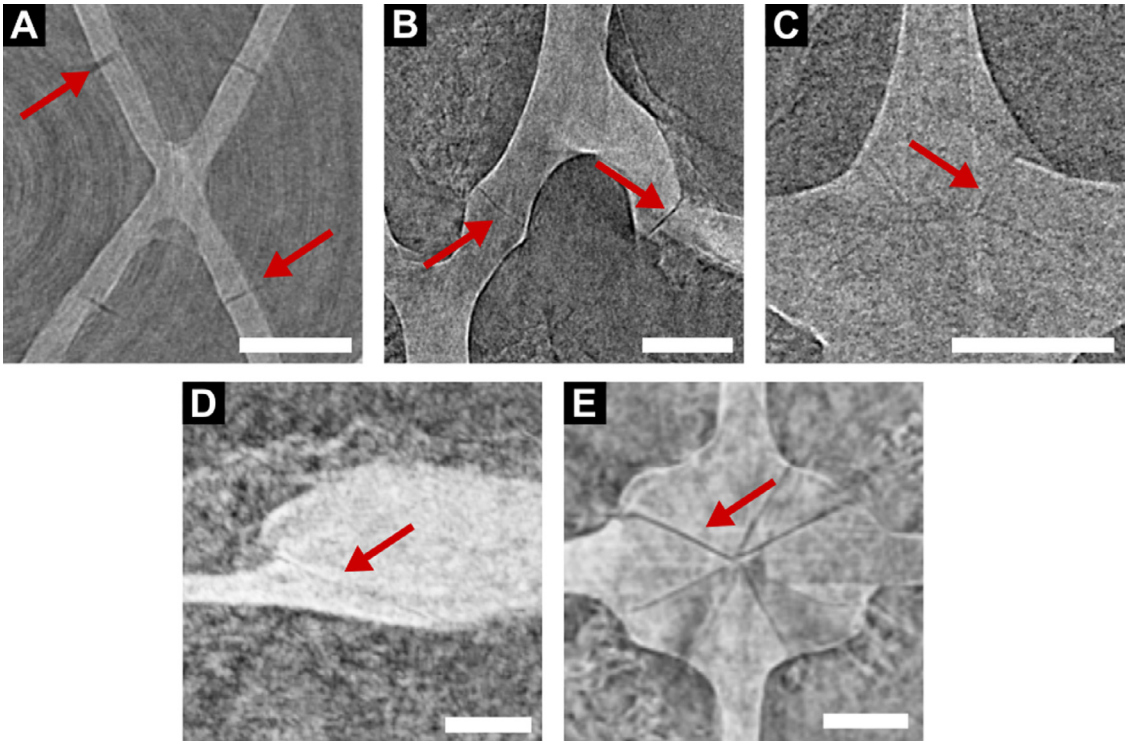


**Fig. 5.** Interspicular interstices (marked with red arrows) are present in Type I-V endoskeletons. (A) Type I: Equatorial spicule in center (B) Type II: Equatorial+tropical (left) and tropical+polar (right)spicule junctions (C) Type III: Polar+equatorial spicule junction (D) Type IV: Tropical spicule and x-shaped equatorial spicule, (E) Type V: Central junction. Scale bars correspond to 5 $\mu$m.

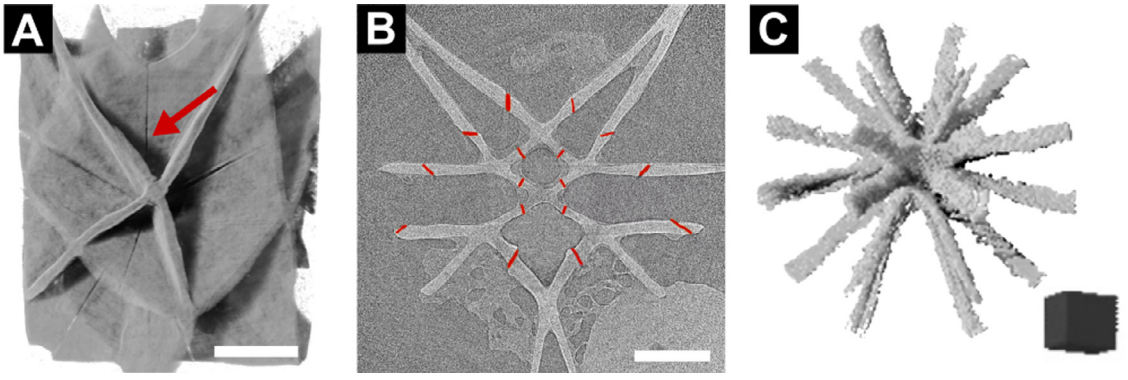


**Fig. 6.** Interstitial space between adjacent spicules. (A) shows one such interstice between lateral wings of adjacent spicules of a Type I sample. The interstices were traced across the reconstructed nanoCT slices as a region of interest as shown in (B) and visualized in (C). Scale bars correspond to 10 µm. Black cube in (C) has side lengths of 2 µm.

**Table 1**
Average angles (º) measured from a central (non-spicule) axis, presented with 95% confidence intervals.

| | TYPE I | TYPE II | TYPE IV | TYPE V | ALL |
|---|---|---|---|---|---|
| Polar | 34.7 ± 0.5 | 35 ± 1.6 | 35.7 ± 0.8 | 35 ± 1.0 | 34.9 ± 0.4 |
| Tropical | 67.6 ± 0.2 | 66.2 ± 0.4 | 68.2 ± 0.2 | 67.3 ± 0.3 | 67.5 ± 0.15 |
| Equatorial | 89.7 ± 0.4 | 87 ± 2 | 89.7 ± 0.4 | 90.7 ± 0.6 | 89.7 ± 0.3 |

The formation of a mineralized endoskeleton offers unique selective advantages to unicellular organisms, ranging from structural support, defense against predators, locomotion, and buoyancy control. The Acantharian endoskeleton present an intriguing example of vesicle bound biomineralization. Growth patterns with high spatial regularity may arise from the internal symmetry of the orthorhombic crystal lattice, as well as geometric constraints in the center of the cell. Yet, pronounced morphological differences exist between taxa, suggesting biologically controlled crystal growth. Interesting parallels can be drawn to more common biomineral systems whose skeletons are based on calcium carbonate or opaline silica. Similar morphological complexity can be found in the fenestrated spicules of tropical sea urchin larvae [52,53] or marine sponges [54]. The curved moieties in some Acantharia resemble the antler spicules of marine ascidians, which are composed of amorphous calcium carbonate [55,56]. While it is yet poorly understood how the curved skeletal elements of the Acantharia are molded, experimental observations have pointed toward the existence of a non-classical crystallization mechanism in biogenic strontium sulfate [57,58]. It is conceivable that Acantharia use mul-

**Table 2**
Average absolute value difference between expected and observed angles as projected onto the equatorial plane, in degrees (º), presented with 95% confidence intervals.

| | Angle difference |
|---|---|
| TYPE I | 3.9 ± 0.3 |
| TYPE II | 7 ± 1.2 |
| TYPE IV | 3.1 ± 0.3 |
| TYPE V | 3.2 ± 0.5 |

tiple strategies in concert to build their intricate mineral skeletons, such as organic crystal growth modifiers and vesicle templating. Other Radiolaria in the eukaryotic supergroup Rhizaria, particularly the centrosymmetric Spumellaria, mineralize siliceous skeletons. Their cortical shells arise from the fusion of radial spicules that do not follow a strict geometric arrangement such as Müller's principle [59,60], indicating that the crystallography does impose limitations on the growth pattern of the Acantharian skeleton.

## 4. Conclusions

In this study, synchrotron-based X-ray nanotomography provides a comprehensive image of the internal skeletal organization and the porous mineralized shell present in some Acantharian species. NanoCT datasets were used to train state-of-the-art deep learning algorithms for image segmentation. Our investigation sheds light on how the spicules emanate from the central junction, the presence and role of lateral spicule wings as well as pockets of interspicular space for possible cell compartmentalization. The cytoplasm, which constitutes the majority of the unicell, is organized around the mineralized structures. Through thorough angle measurements across species, we detected minor, but statistically significant deviations from Müller's principle and diverse patterns of spicule connectivity. We further observed changes in spicule shape along diametrically aligned spicules across different types and investigated the requirements of spatial arrangements that might restrict spicular shapes. We discuss the role of lateral wings and porous shells to strengthen and support the skeletal structure. Overall, this morphological information contributes to a better understanding of the skeletal development and morphogenesis resulting in the unparalleled diversity of Acantharian endoskeletons. This study is highly original since it focuses on celestite as yet poorly explored biomineral system. Understanding how complex bioinorganic structures are formed is of significant interest for solid-state chemistry, bioinorganic chemistry and nanotechnology, specifically for developing low-temperature synthesis routes and fracture-resistant ceramics. Many of the bio-inspired approaches towards single crystals with complex shape have not been attempted for celestite. Potential industrial applications of earth alkaline sulfates are the reduction of barite scales in oilfield operations [61], the selective removal of strontium-90 radioisotopes from nuclear waste [62], celestite-based radiation dosimeters [63], strontium-substituted bioceramics as bone replacement materials [64], or $SrSO_4$ coatings as high-temperature solid lubricant [65].

## Author contribution

V.M. conceived the idea of the study and carried out the X-ray nanoCT experiments. D.R.S. and T.C. produced 3D models of the skeletons. D.R.S. analyzed the data using deep learning segmentation and measured inter-spicule angles. E.L. and I. G. assisted with the data acquisition and reconstructed the tomographic datasets. D.R.S. and V.M. drafted the manuscript. All authors contributed to the interpretation of the results and commented on the manuscript.

## Declaration of Competing Interest

The authors declare that they have no known competing financial interests or personal relationships that could have appeared to influence the work reported in this paper.

## Acknowledgements

We acknowledge DESY (Hamburg, Germany), a member of the Helmholtz Association HGF, for the provision of experimental facilities. Parts of this research were carried out at PETRA III. Beamtime was allocated for proposal I-20190413. Portions of this work were performed DND-CAT located at Sector 5. DND-CAT is supported by Northwestern University, E. I. DuPont de Nemours & Co., and The Dow Chemical Company. We acknowledge Mike Guise and Denise Keane for technical support at the 5-BM-C beamline. We thank John Burns and Eunsoo Kim from the American Museum of Natural History in New York for providing plankton assemblage samples. Dr. Merk thanks the National Science Foundation (NSF 2137663, Division of Materials Research) and the Swiss National Science Foundation for an Early Postdoc Mobility Fellowship for financial support.

## Supplementary materials

Supplementary material associated with this article can be found, in the online version, at doi:10.1016/j.actbio.2023.01.037.

## References

[1] G.A. Ozin, Morphogenesis of biomineral and morphosynthesis of biomimetic forms, Acc. Chem. Res. 30 (1997) 17–27, doi:10.1021/ar960021r.
[2] H. Yang, N. Coombs, G.A. Ozin, Morphogenesis of shapes and surface patterns in mesoporous silica, Nature 386 (1997) 692–695, doi:10.1038/386692a0.
[3] N. Coombs, D. Khushalani, S. Oliver, G.A. Ozin, G. Cheng Shen, I. Sokolov, H. Yang, Blueprints for inorganic materials with natural form: inorganic liquid crystals and a language of inorganic shape†, J. Chem. Soc. Dalt. Trans. (1997) 3941–3952, doi:10.1039/A704741J.
[4] S. Mann, G.A. Ozin, Synthesis of inorganic materials with complex form, Nature 382 (1996) 313–318.
[5] A. Aziz, J. Carrasco, Towards predictive synthesis of inorganic materials using network science, Front. Chem. 9 (2021) https://www.frontiersin.org/article/10.3389/fchem.2021.798838.
[6] B. Wucher, W. Yue, A.N. Kulak, F.C. Meldrum, Designer crystals: single crystals with complex morphologies, Chem. Mater. 19 (2007) 1111–1119, doi:10.1021/cm0620640.
[7] H. Li, H.L. Xin, D.A. Muller, L.A. Estroff, Visualizing the 3D Internal structure of calcite single crystals grown in agarose hydrogels, Science 326 (2009) 1244 LP –1247, doi:10.1126/science.1178583.
[8] L. Addadi, J. Aizenberg, E. Beniash, S. Weiner, On the concept of a single crystal in biomineralization, in: D. Braga, F. Grepioni, A.G. Orpen (Eds.), Crystal Engineering: From Molecules and Crystals to Materials, Springer, Netherlands, Dordrecht, 1999, pp. 1–22, doi:10.1007/978-94-011-4505-3_1.
[9] I. Sunagawa, in: Single Crystals Grown Under Unconstrained Conditions, Springer Handb. Cryst. Growth, 2010, pp. 133–157, doi:10.1007/978-3-540-74761-1_5.
[10] M. Koifman Khristosov, L. Kabalah-Amitai, M. Burghammer, A. Katsman, B. Pokroy, Formation of curved micrometer-sized single crystals, ACS Nano 8 (2014) 4747–4753, doi:10.1021/nn5013513.
[11] F. Nudelman, N.A.J.M. Sommerdijk, Biomineralization as an inspiration for materials chemistry, Angew. Chemie Int. Ed. 51 (2012) 6582–6596, doi:10.1002/anie.201106715.
[12] S.V. Auras, L.B.F. Juurlink, Recent advances in the use of curved single crystal surfaces, Prog. Surf. Sci. 96 (2021) 100627, doi:10.1016/j.progsurf.2021.100627.
[13] G. Paterno, V. Bellucci, R. Camattari, V. Guidi, Design study of a Laue lens for nuclear medicine, J. Appl. Crystallogr. 48 (2015) 125–137, doi:10.1107/S1600576714026235.
[14] J. Müller, Über die thalassicollen, polycystinen und acanthometren des mittelmeeres, Abh Akad Wiss Berlin (1858).
[15] F. Gómez, K. Kiriakoulakis, E. Lara, Achradina pulchra, a Unique Dinoflagellate (Amphilothales, Dinophyceae) with a radiolarian-like endoskeleton of celestite (Strontium Sulfate), Acta Protozool. 56 (2) (2017) https://www.ejournals.eu/Acta-Protozoologica/2017/Issue-2/art/10270/.
[16] L.A. Zettler, M.L. Sogin, D.A. Caron, Phylogenetic relationships between the Acantharea and the Polycystinea: a molecular perspective on Haeckel's Radiolaria, Proc. Natl. Acad. Sci. 94 (1997) 11411–11416.

[17] S. Schultze-Lam, T.J. Beveridge, Nucleation of celestite and strontianite on a cyanobacterial s-layer, Appl. Environ. Microbiol. 60 (1994) 447–453, doi:10.1128/aem.60.2.447-453.1994.
[18] M. Mars Brisbin, O.D. Brunner, M.M. Grossmann, S. Mitarai, Paired high-throughput, in situ imaging and high-throughput sequencing illuminate acantharian abundance and vertical distribution, Limnol. Oceanogr. 65 (2020) 2953–2965, doi:10.1002/lno.11567.
[19] R.E. Bernstein, P.R. Betzer, R.A. Feely, R.H. Byrne, M.F. Lamb, A.F. Michaels, Acantharian fluxes and strontium to chlorinity ratios in the North Pacific Ocean, Science 237 (1987) 1490–1494.
[20] R.E. Bernstein, R.H. Byrne, P.R. Betzer, A.M. Greco, Morphologies and transformations of celestite in seawater: the role of acantharians in strontium and barium geochemistry, Geochim. Cosmochim. Acta. 56 (1992) 3273–3279.
[21] P. Martin, J.T. Allen, M.J. Cooper, D.G. Johns, R.S. Lampitt, R. Sanders, D.A.H. Teagle, Sedimentation of acantharian cysts in the Iceland Basin: strontium as a ballast for deep ocean particle flux, and implications for acantharian reproductive strategies, Limnol. Oceanogr. 55 (2010) 604–614, doi:10.4319/lo.2010.55.2.0604.
[22] J. Decelle, P. Martin, K. Paborstava, D.W. Pond, G. Tarling, F. Mahé, C. De Vargas, R. Lampitt, F. Not, Diversity, ecology and biogeochemistry of cyst-forming Acantharia (Radiolaria) in the oceans, PLoS ONE 8 (2013) e53598.
[23] Ernst Haeckel, Report On the Radiolaria Collected By H.M.S. Challenger During the Years 1873-1876: Porulosa (Spumellaria and Acantharia) and Subclass Osculosa, 1st ed., Eyre & Spottiswoode, London, 1887.
[24] V.T. Shevîakov, Die Acantharia Des Golfes Von Neapel, Fauna e fl, G. Bardi, Roma, Roma, 1926.
[25] E. Haeckel, Die Radiolarien (Rhizopoda radiaria), G. Reimer, Eine MonographieBerlin, 1862 https://www.biodiversitylibrary.org/item/40590.
[26] C.C. Perry, J.R. Wilcock, R.J.P. Williams, A physico-chemical approach to morphogenesis: the roles of inorganic ions and crystals, Experientia 44 (1988) 638–650.
[27] J.R. Wilcock, C.C. Perry, R.J.P. Williams, R.F.C. Mantoura, Crystallographic and morphological studies of the celestite skeleton of the acantharian species Phyllostaurus siculus, Proc. R. Soc. London. Ser. B. Biol. Sci. 233 (1988) 393–405.
[28] D.W. Thompson, On Growth and Form, Cambridge University Press, Cambridge, 1917, doi:10.1017/CBO9781107325852.
[29] S. Mann, C.C. Perry, Solid-state bioinorganic chemistry: mechanisms and models of biomineralization, Adv. Inorg. Chem. 36 (1991) 137–200, doi:10.1016/S0898-8838(08)60039-2.
[30] E.M. Bottazzi, A. Vinci, Verifica della legge di Muller e Osservazioni sulla struttura mineralogica delle spicole degli Acantari (Protozoa). Atenco Parmense, Acta Nat. (1965) 3–12.
[31] N. Suzuki, Y. Aita, Radiolaria: achievements and unresolved issues: taxonomy and cytology, Plankt. Benthos Res. 6 (2011) 69–91.
[32] S.C. Benson, N.C. Benson, F. Wilt, The organic matrix of the skeletal spicule of sea urchin embryos, J. Cell Biol. 102 (1986) 1878–1886, doi:10.1083/jcb.102.5.1878.
[33] S. Mann, Biomineralization: Principles and Concepts in Bioinorganic Materials Chemistry, Oxford University Press on Demand, Oxford, 2001.
[34] J. Decelle, F. Not, Acantharia, ELS (2015) 1–10.
[35] A.F. Michaels, Vertical distribution and abundance of Acantharia and their symbionts, Mar. Biol. 97 (1988) 559–569, doi:10.1007/BF00391052.
[36] E.J. Reardon, D.K. Armstrong, Celestite (SrSO4(s)) solubility in water, seawater and NaCl solution, Geochim. Cosmochim. Acta. 51 (1987) 63–72.
[37] D.J. Gifford, D.A. Caron, 5 - Sampling, Preservation, Enumeration and Biomass of Marine Protozooplankton, in: R. Harris, P. Wiebe, J. Lenz, H.R. Skjoldal, M.B.T.-I.Z.M.M. Huntley (Eds.), Academic Press, London, 2000: pp. 193–221. https://doi.org/10.1016/B978-012327645-2/50006-2.
[38] J. Decelle, G. Veronesi, B. Gallet, H. Stryhanyuk, P. Benettoni, M. Schmidt, R. Tucoulou, M. Passarelli, S. Bohic, P. Clode, Subcellular chemical imaging: new avenues in cell biology, Trends Cell Biol. 30 (2020) 173–188.
[39] P.J. Withers, X-ray nanotomography, Mater. Today. 10 (2007) 26–34.
[40] T. Beuvier, I. Probert, L. Beaufort, B. Suchéras-Marx, Y. Chushkin, F. Zontone, A. Gibaud, X-ray nanotomography of coccolithophores reveals that coccolith mass and segment number correlate with grid size, Nat. Commun. 10 (2019) 751, doi:10.1038/s41467-019-08635-x.
[41] V. Schoeppler, E. Reich, J. Vacelet, M. Rosenthal, A. Pacureanu, A. Rack, P. Zaslansky, E. Zolotoyabko, I. Zlotnikov, Shaping highly regular glass architectures: a lesson from nature, Sci. Adv. 3 (2017) eaao2047.
[42] H.J.H. Johnstone, M. Schulz, S. Barker, H. Elderfield, Inside story: an X-ray computed tomography method for assessing dissolution in the tests of planktonic foraminifera, Mar. Micropaleontol. 77 (2010) 58–70.
[43] S. Holst, P. Michalik, M. Noske, J. Krieger, I. Sötje, Potential of X-ray micro–computed tomography for soft-bodied and gelatinous cnidarians with special emphasis on scyphozoan and cubozoan statoliths, J. Plankton Res. 38 (2016) 1225–1242.
[44] I. Greving, F. Wilde, M. Ogurreck, J. Herzen, J. Hammel, A. Hipp, F. Friedrich, L. Lottermoser, T. Dose, H. Burmester, M. Mueller, F. Beckmann, P05 imaging beamline at PETRA III: first results, Opt. Photonics - Opt. Eng. + Appl., 2014.
[45] S. Flenner, M. Storm, A. Kubec, E. Longo, F. Doring, D.M. Pelt, C. David, M. Muller, I. Greving, Pushing the temporal resolution in absorption and Zernike phase contrast nanotomography: enabling fast in situ experiments, J. Synchrotron Radiat. 27 (2020) 1339–1346, doi:10.1107/S1600577520007407.
[46] B. Dowd, G. Campbell, R. Marr, V. Nagarkar, S. Tipnis, L. Axe, D. Siddons, Developments in synchrotron x-ray computed microtomography at the National Synchrotron Light Source, Opt. Photonics (1999).
[47] D. Gürsoy, F. De Carlo, X. Xiao, C. Jacobsen, TomoPy: a framework for the analysis of synchrotron tomographic data, J. Synchrotron Radiat. 21 (2014) 1188–1193, doi:10.1107/S1600577514013939.
[48] Ronneberger, O., Fischer, P. & Brox, T. U-Net: Convolutional Networks for Biomedical Image Segmentation BT - Medical Image Computing and Computer-Assisted Intervention – MICCAI 2015. in (eds. Navab, N., Hornegger, J., Wells, W. M. & Frangi, A. F.) 234–241 (Springer International Publishing, 2015).
[49] A. Fedorov, R. Beichel, J. Kalpathy-Cramer, J. Finet, J.-C. Fillion-Robin, S. Pujol, C. Bauer, D. Jennings, F. Fennessy, M. Sonka, J. Buatti, S. Aylward, J.V. Miller, S. Pieper, R. Kikinis, 3D Slicer as an image computing platform for the Quantitative Imaging Network, Magn. Reson. Imaging. 30 (2012) 1323–1341, doi:10.1016/j.mri.2012.05.001.
[50] R. Fujimaki, N. Suzuki, K. Kimoto, Y. Nagai, Y. Oaki, S. Shimode, T. Toyofuku, H. Imai, Micro- and nanometric characterization of the celestite skeleton of acantharian species (Radiolaria, Rhizaria), Sci. Rep. 12 (2022) 2848, doi:10.1038/s41598-022-06974-2.
[51] H. Haimov, E. Shimoni, V. Brumfeld, M. Shemesh, N. Varsano, L. Addadi, S. Weiner, Mineralization pathways in the active murine epiphyseal growth plate, Bone 130 (2020) 115086, doi:10.1016/j.bone.2019.115086.
[52] F.H. Wilt, Biomineralization of the Spicules of Sea Urchin Embryos, Zoolog. Sci. 19 (2002) 253–261, doi:10.2108/zsj.19.253.
[53] R.B. Emlet, Larval spicules, cilia, and symmetry as remnants of indirect development in the direct developing sea urchin heliocidaris erythrogramma, Dev. Biol. 167 (1995) 405–415, doi:10.1006/dbio.1995.1037.
[54] W.E.G.B.T.-I.R. of C. X. Wang, H.C. Schröder, M.B. Müller, in: Chapter 3 Giant Siliceous Spicules From the Deep-sea Glass Sponge Monorhaphis Chuni, Academic Press, 2009, pp. 69–115, doi:10.1016/S1937-6448(08)01803-0.
[55] G. Lambert, Spicule formation in the solitary ascidian Bathypera feminalba (Ascidiacea, Pyuridae), Invertebr. Biol. (1998) 341–349.
[56] G. Lambert, C.C. Lambert, Spicule formation in the New Zealand Ascidian Pyura pachydermatina (Chordata, Ascidiacea), Connect. Tissue Res. 34 (1996) 263–269, doi:10.3109/03008209609005270.
[57] S. Otani, Crystal habit modification of strontium sulfate. I. Habit-modifying action of foreign substances, Bull. Chem. Soc. Jpn. 33 (1960) 1543–1548, doi:10.1246/bcsj.33.1543.
[58] R. Fujimaki, Y. Oaki, H. Imai, A nonclassical pathway to biomimetic strained SrSO4 crystals, CrystEngComm 24 (2022) 4356–4360, doi:10.1039/D2CE00379A.
[59] T. Biard, Diversity and ecology of Radiolaria in modern oceans, Environ. Microbiol. 24 (2022) 2179–2200, doi:10.1111/1462-2920.16004.
[60] M.S. Afanasieva, E.O. Amon, Symmetry in radiolarian skeletons: rules and exceptions, Paleontol. J. 48 (2014) 1163–1171, doi:10.1134/S0031030114110021.
[61] R.D. Sosa, X. Geng, A. Agarwal, J.C. Palmer, J.C. Conrad, M.A. Reynolds, J.D. Rimer, Acidic polysaccharides as green alternatives for barite scale dissolution, ACS Appl. Mater. Interfaces. 12 (2020) 55434–55443, doi:10.1021/acsami.0c16653.
[62] P. Misaelides, Separation of Cesium-137, Strontium-90 and Actinides from waters and wastewaters: a short review of the materials and processes, in: M. Václavíková, K. Vitale, G.P. Gallios, L. Ivaničová (Eds.), Water Treatment Technologies For the Removal of High-Toxicity Pollutants, Springer Netherlands, Dordrecht, 2010, pp. 183–191.
[63] M.A.H. Rushdi, A.A. Abdel-Fattah, M.M. Sherif, Y.S. Soliman, A. Mansour, Strontium sulfate as an EPR dosimeter for radiation technology application, Radiat. Phys. Chem. 106 (2015) 130–135, doi:10.1016/j.radphyschem.2014.07.009.
[64] R.D. Prabha, M. Ding, P. Bollen, N. Ditzel, H.K. Varma, P.D. Nair, M. Kassem, Strontium ion reinforced bioceramic scaffold for load bearing bone regeneration, Mater. Sci. Eng. C. 109 (2020) 110427.
[65] T. Murakami, K. Umeda, S. Sasaki, J. Ouyang, High-temperature tribological properties of strontium sulfate films formed on zirconia-alumina, alumina and silicon nitride substrates, Tribol. Int. 39 (2006) 1576–1583.